Intensity-based readout of resonant-waveguide grating biosensors: systems and nanostructures

Moritz Paulsen, Sabrina Jahns, Martina Gerken

Institute of Electrical Engineering and Information Technology, Kiel University,
Kaiserstr. 2, 24143 Kiel, Germany

Abstract

Resonant waveguide gratings (RWG) – also called photonic crystal slabs (PCS) – have been established as reliable optical transducers for label-free biochemical assays as well as for cell-based assays. Current readout systems are based on mechanical scanning and spectrometric measurements with system sizes suitable for laboratory equipment. Here, we review recent progress in compact intensity-based readout systems for point-of-care (POC) applications. We briefly introduce PCSs as sensitive optical transducers and introduce different approaches for intensity-based readout systems. Photometric measurements have been realized with a simple combination of a light source and a photodetector. Recently a 96-channel, intensity-based readout system for both biochemical interaction analyses as well as cellular assays was presented employing the intensity change of a near cut-off mode. As an alternative for multiparametric detection, a camera system for imaging detection has been implemented. A portable, camera-based system of size 13 cm x 4.9 cm x 3.5 cm with six detection areas on an RWG surface area of 11 mm x 7 mm has been demonstrated for the parallel detection of six protein binding kinetics. The signal-to-noise ratio of this system corresponds to a limit of detection of 168 pM (24 ng/ml). To further improve the signal-to-noise ratio advanced nanostructure designs are investigated for RWGs. Here, results on multiperiodic and deterministic aperiodic nanostructures are presented. These advanced nanostructures allow for the design of the number and wavelengths of the RWG resonances. In the context of intensity-based readout systems they are particularly interesting for the realization of multi-LED systems. These recent trends suggest that compact point-of-care systems employing disposable test chips with RWG functional areas may reach market in the near future.

1. Introduction

In the last years, the detection of proteins as one type of biomarker has become more and more important in diagnostics of slowly progressing diseases as well as for acute cases [1, 2]. Thereby the detection of multiple proteins is often needed for unambiguous diagnosis. For the detection of multiple protein levels in blood, typically a blood sample is analyzed in a central laboratory using, e.g., ELISA (enzyme-linked immunosorbent assay) tests. Currently, there is a strive towards decentralized point-of-care (POC) analysis systems that allow for detection of the relevant protein levels in small sample volumes to ensure regular and fast diagnosis. Several systems for POC biomarker detection are already on the market including, e.g., pregnancy tests, glucose tests, the *Roche TROP T® sensitive-test* (Roche Deutschland Holding GmbH) for troponin detection or the iron self-test *STADA Diagnostik Eisen* (STADApharm GmbH). Multiple-protein measurements from a single sample still pose a challenge and a variety of systems is currently under investigation. Biosensors may be classified by the technology of their three constitutive parts: the selective and specific biological recognition component (receptor), the signal transducer, and the data evaluation. The bio-chemical receptor is directly connected to the transducer and enables the specific and unambiguous binding of protein target molecules. The transducer transforms this binding into a detectable signal. This transformation can be performed, e.g., mechanically [3], electrochemically [4], optically [5], or with surface acoustic wave sensors [6]. Optical biosensors offer the advantage of a physical separation of the transducer with the biological recognition component, which is in contact with the sample, and the optical detection hardware with the electronics and the data evaluation. A non-contact, free-space optical link allows for the combination of one-way

test chips with a separate detection system. Figure 1 (a, b) depicts a scheme using out-of-plane illumination of a one-way chip for parallel detection of multiple proteins.
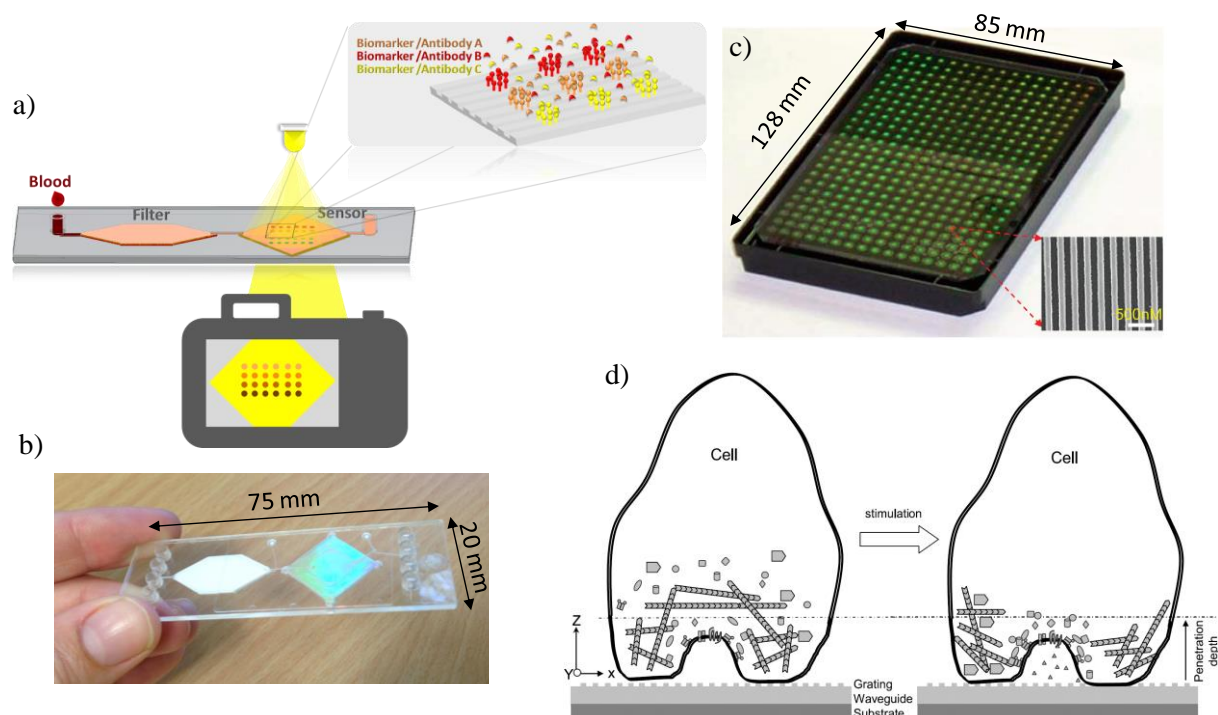

Figure 1. (a) Point-of-care (POC) sensor concept with one-way microfluidic detection chip and camera-based readout system for multiple protein detection [reproduced from [30] with permission (will be obtained after acceptance of manuscript)]. (b) Microfluidic chip prototype with filter unit and detection field. (c, d) 384-well biosensor microplate (Epic® system, Corning Inc.) and schematic of nanostructured waveguide with cell showing mass redistribution upon stimulation [reproduced from [13] with permission (will be obtained after acceptance of manuscript)].

Today, most of the optical approaches use label-based detection schemes such as fluorescence assays [7]. For point-of-care systems, label-free detection is of particular interest as additional reagents and preparation steps are not required [8]. Label-free optical transducers studied in the past range from waveguide interferometry [9] and surface plasmon resonances [10] to micro ring resonators [11] and photonic crystal sensors [12]. Nanostructured surfaces such as resonant waveguide gratings allow for coupling of the transducer with out-of-plane illumination without additional coupling structures. Figure 1c) shows the photograph of a commercially available 384-well biosensor microplate with a nanostructured well bottom (Epic® system, Corning Inc.). Currently, a spectrometer-based readout scheme is utilized in commercial systems with broadband illumination [13]. Imaging angle-based readout has been demonstrated using a laser as the light source [14]. These label-free systems may be employed for biochemical assays as well as for cell-based assays. In cell-based assays the mass change at the surface of the nanostructured waveguide is detected, which may be linked to a change in the cell number or size or a dynamic mass redistribution (DMR) in cells upon a stimulus (see Figure 1d).

An overview of emerging photonic crystal biosensors is found in references [15] and [16]. In this review we discuss the intensity-based readout of resonant waveguide grating sensors, also called photonic crystal sensors. For an intensity-based readout no spectrometer or angle-scanning mechanics are needed. Therefore, this detection scheme offers high potential for the miniaturization of the complete optical system – not just the detection volume. On the other hand, an intensity-based system is more susceptible to background effects. For cell-based assays, the question of optical scattering losses due to cells is of particular importance. In biochemical assays the separation of signal and background drift needs to be considered. Section 2 explains the principles of guided-mode resonances for optical biosensing. In section 3, intensity-based system designs are presented and the state-of-the-art performance is discussed. Subsequently in section 4, new developments on multiperiodic and deterministic aperiodic nanostructures for resonant waveguide grating sensors are introduced. A summary and an outlook are given in section 5.

2. Photonic Crystal Slabs (PCS) as Sensitive Optical Transducers

Resonant waveguide gratings (RWG) with one- or two-dimensionally periodic nanostructures as depicted schematically in Figure 2a are also called photonic crystal slabs (PCS). Here, double-grating nanostructures are considered with gratings on both sides of the waveguide. These model samples obtained by a nanoimprint-lithography process on the substrate and subsequent waveguide layer deposition by sputtering. The sub-wavelength nanostructure serves as a grating coupler coupling out-of-plane incident light to the waveguide layer and light from quasi-guided modes to radiation modes. Due to the leakage of the guided light to radiation, the waveguide modes are called quasi-guided modes. For the waveguide layer to be able to guide light, its refractive index (n_2) must be higher than that of the substrate (n_3) and that of the surrounding medium (n_1), also referenced as cladding or analyte region. Following this condition, the waveguide is often called high-index layer. At certain wavelengths, the light reflected from the nanostructured waveguide layer interferes constructively in reflection and reflection peaks are observed at these guided-mode resonances (GMR). Simultaneously, dips appear in the transmission spectrum. Due to interference effects of different propagations paths, the guided-mode resonances have a Fano-type line shape [17]. Allowing for transverse-electric modes (TE case, electric field component in the plane of the waveguide) and transverse-magnetic modes (TM case, magnetic field vector in the plane of the waveguide), PCSs have distinct resonances for the two polarizations, that may be addressed by the polarization of the incident light. We use a transmission confocal microscope setup to characterize samples. To excite either transverse electric (TE) or transverse magnetic (TM) guided-mode resonances a polarization filter is used and the polarization is changed by either turning the sample or the filter by 90° degrees. The transmitted light is collected and coupled to a spectroscope (Shamrock 500i, Andor) with a CCD camera (Andor). The recorded transmission spectra are normalized to the recorded spectrum of the broadband halogen illumination source. Two typical transmission spectra of a PCS with a period of 370 nm and a titanium dioxide high-index layer are depicted in figure 2 b), showing the TE_0 guided-mode resonance and the TM_0 guided-mode resonance. Distinct minima are visible at 540 nm for the TM case and 585 nm for the TE case.

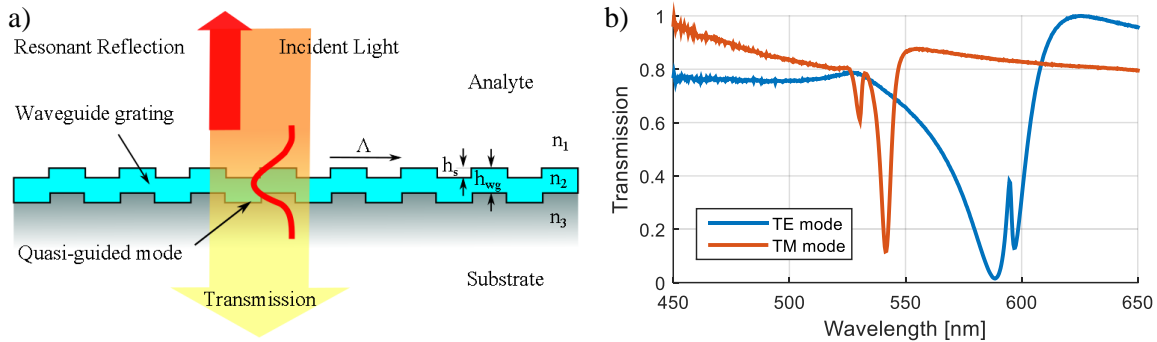

Figure 2 (a) Out-of-plane illumination couples to a quasi-guided mode of a nanostrucuted waveguide. At particular wavelengths, resonant reflection is observed causing dips in the transmission spectrum. b) Examples of experimentally-observed transmission spectra in TE and TM polarization for a photonic crystal slab with a TiO_2 waveguiding layer and a 370-nm period. The substrate is glass and the analyte is air.

Following Bragg theory, the resonance wavelength λ_{res} is a function of the grating period Λ, the effective refractive index n_{eff} of the guided mode and the angle of incidence Θ [18]:

$$\lambda_{res} = \Lambda \cdot (n_{eff} \pm \sin(\Theta)) \qquad (1)$$

The grating allows for light coupling into forward- and backward-propagating modes, corresponding to the $\pm\sin(\Theta)$ term. At normal incidence, the resonance position becomes a mere function of the grating period and the effective refractive index of the quasi-guided mode. Here the forward- and backward-propagating modes interfere destructively and open up the $\Lambda/2$ band gap known from 1-dimensional photonic crystals [19]. Note that the resonance splitting observed in figure 2b is caused by the irradiation cone of ± 2° in our setup. For perfect normal incidence only a single dip is observed corresponding to one of the band edges with the other band edge being dark. For higher angles two dips are observed following equation (1). The illumination cone of our microscope setup is limited by a pinhole in front of the halogen illumination lamp. Thus, the spectrum is averaged over the irradiation cone.

As depicted in figure 2 a), the quasi-guided mode has evanescent parts in the cladding and substrate regions und thus the effective refractive index is a function of the geometric and the material properties of the structure and the surrounding media. Changes in the refractive index of the analyte region will lead to a change in the resonance wavelength $\Delta\lambda_{res}$ and a frequency change $\Delta\omega_{res}$, respectively. $\Delta\lambda_{res}$ and $\Delta\omega_{res}$ depend on the overlap of the electric field with the refractive index change as described by J. Yang, H. Giessen, and P. Lalanne [20]

$$\Delta\omega_{res} = -\omega_{res} \iiint_{V_p} \Delta\varepsilon(r,\omega) \, \widetilde{E}_{app}(r) \cdot \widetilde{E}(r) \mathrm{d}^3 r \qquad (2)$$

In equation (2), V_p is the volume experiencing a refractive index perturbation, $\Delta\varepsilon$ is the change in dielectric constant due to the perturbation, $\widetilde{E}$ the unperturbed electric field vector of the quasi-normalized mode, and $\widetilde{E}_{app}$ the approximate perturbed normalized electric field vector. For a high sensitivity, a large electric field overlap with the volume of changed refractive index is necessary. The sensitivity S is defined as the quotient of the resonance shift and the change of refractive index in the analyte region:

$$S = \frac{\Delta\lambda_{res}}{\Delta n_1}. \qquad (3)$$

The energy stored in a resonator is linked to the quality factor of the resonance, which is defined by [21]:

$$Q = \frac{\lambda_{res}}{\mathrm{FWHM}}. \qquad (4)$$

If target biomarkers bind to the specific receptor on the sensor surface, the refractive index is locally changed and the binding thus leads to a shift in the resonance position. It is distinguished between bulk sensitivity and surface sensitivity. Bulk sensitivity considers a change in refractive index for the whole analyte region. Surface sensitivity assumes a refractive index change in a thin layer close to the structure surface [22-24].

We simulate the performance of different photonic crystal slabs using the simulation tool FDTD Solutions (finite difference time domain, Lumerical Solutions, Inc.) and COMSOL Multiphysics® (finite element method, FEM). A comparative study of three simulation methods for nanostructured dielectric waveguides has recently been published, marking FDTD, FEM and RCWA (rigorous-coupled wave analysis) as suitable simulation tools for this purpose [25]. Figure 3 shows examples of the electric field distribution on resonance for TE and TM polarization. From Figure 3 a higher sensitivity is expected for TM polarization as the field fill factor in the analyte is higher.
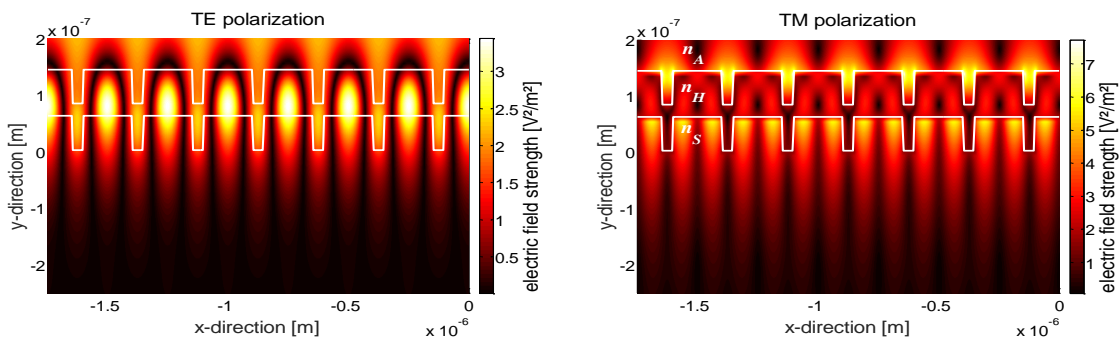

Figure 3: FDTD simulated electric field strengths of a) TE and b) TM guided mode resonance for excitation at normal incidence. The nanostructured waveguide outline is shown in white. The period is Λ = 250 nm, the structure depth 60 nm, n_a= 1.00, n_s=2.48 and n_h= 1.52.

To consider effects of the penetration depth in some more detail, figure 4a shows the calculated mode profiles in a 100-nm thick waveguide layer for wavelengths ranging from 400 nm to 700 nm. In this simulation we consider the waveguide without the nanostructure for simplicity. An evanescent-field penetration depth of about 40 nm to 90 nm into the air analyte region on the left is observed for this geometry. The modes of shorter wavelengths have a tighter confinement to the waveguide. Due to the confinement of the mode to the waveguide, photonic-crystal slabs are only sensitive to refractive index changes close to the surface. This is highly advantageous for suppression of background effects in the

sample volume. On the other hand, for cell experiments such as the one depicted in figure 1d, a larger penetration depth may be needed. Thus, designs are of interest that push the electric field into the analyte such as the reverse-symmetry waveguides suggested by R. Horvath et al. [22].
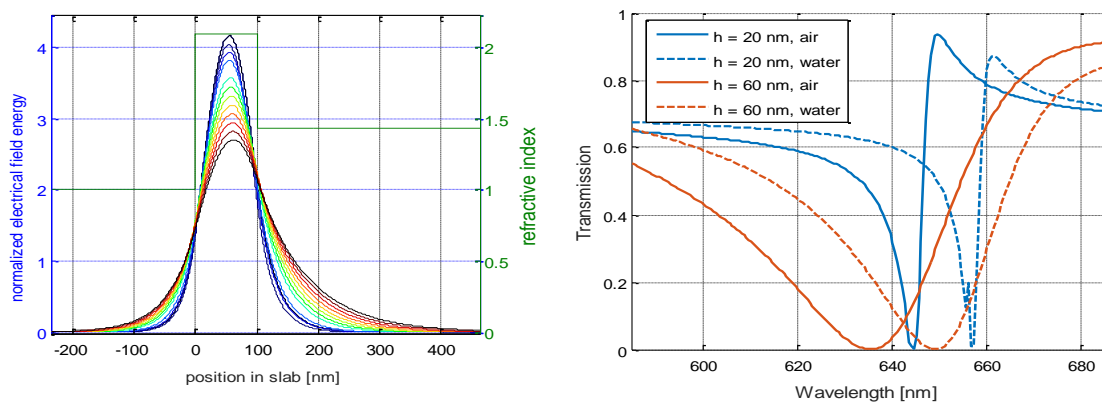

Figure 4: a) Calculated TE_0 mode profiles for wavelengths ranging from 400 nm to 700 nm (colorcoded blue to red) of a 100-nm thick high-index layer ($n_2 = 2.2$) on a quartz substrate. Shorter wavelengths show higher confinement. b) FEM simulation of a 370-nm grating with a 70-nm TiO_2 high-index layer and two different structure depths of 20 nm and 60 nm for two different analytes (air, water).

Next, the influence of the nanostructure depth on the resonance spectra is discussed. Figure 4b plots the simulated TE transmission spectra for two different structure depths of 20 nm and 60 nm. The Fano-type line shape is clearly visible. For shallow gratings, a higher quality factor is observed. Deeper gratings cause larger scattering losses. As scattering losses are the dominant loss factor in these dielectric gratings, the stored energy in the resonator is reduced correspondingly, the quality factor is smaller, and the resonance linewidth is larger following equation (4). While the sensitivity is a mere function of the field distribution, a higher Q has no impact on the resonance shift, as seen in figure 4 b. This is in contrast to PCSs that are used for fluorescence enhancement, which is a function of the field intensity [26]. For intensity-based measurement setups, an intermediate quality factor of around Q ~ 160 has proven advantageous for combining a significant intensity change and a good signal-to-noise ratio.

3. Intensity-based PCS readout systems

3.1. Single-channel intensity-based PCS system

In the simplest case, an intensity-based, single-channel PCS readout system requires only a light-emitting diode (LED) and an optical detector. As discussed in section 2 a refractive index change at the surface causes a wavelength shift of the guided-mode resonance. Placing the guided-mode resonance on one of the edges of the LED emission spectrum, this wavelength shift is converted to a change in the transmitted intensity. The signal-to-noise ratio (SNR) may be improved significantly by the integration of two crossed polarization filters [27]. As shown in figure 5 these crossed polarization filters are placed before and after the PCS. Background light not interacting with the PCS and not experiencing any other change in polarization direction is blocked by the second polarizer. Light coupled into the quasi-guided mode in the PCS by the grating structure has a new polarization direction determined by the grating. Thus, light transmitted through the PCS at resonance can pass the second polarizer. Nazirizadeh et al. [27] realized a compact intensity-based readout system capable of detecting 2.5 nM of the protein streptavidin (66 kDa) with a biotinylated surface. The signal-to-noise ratio corresponds to a limit of detection of 280 pM (18,4 ng/ml).
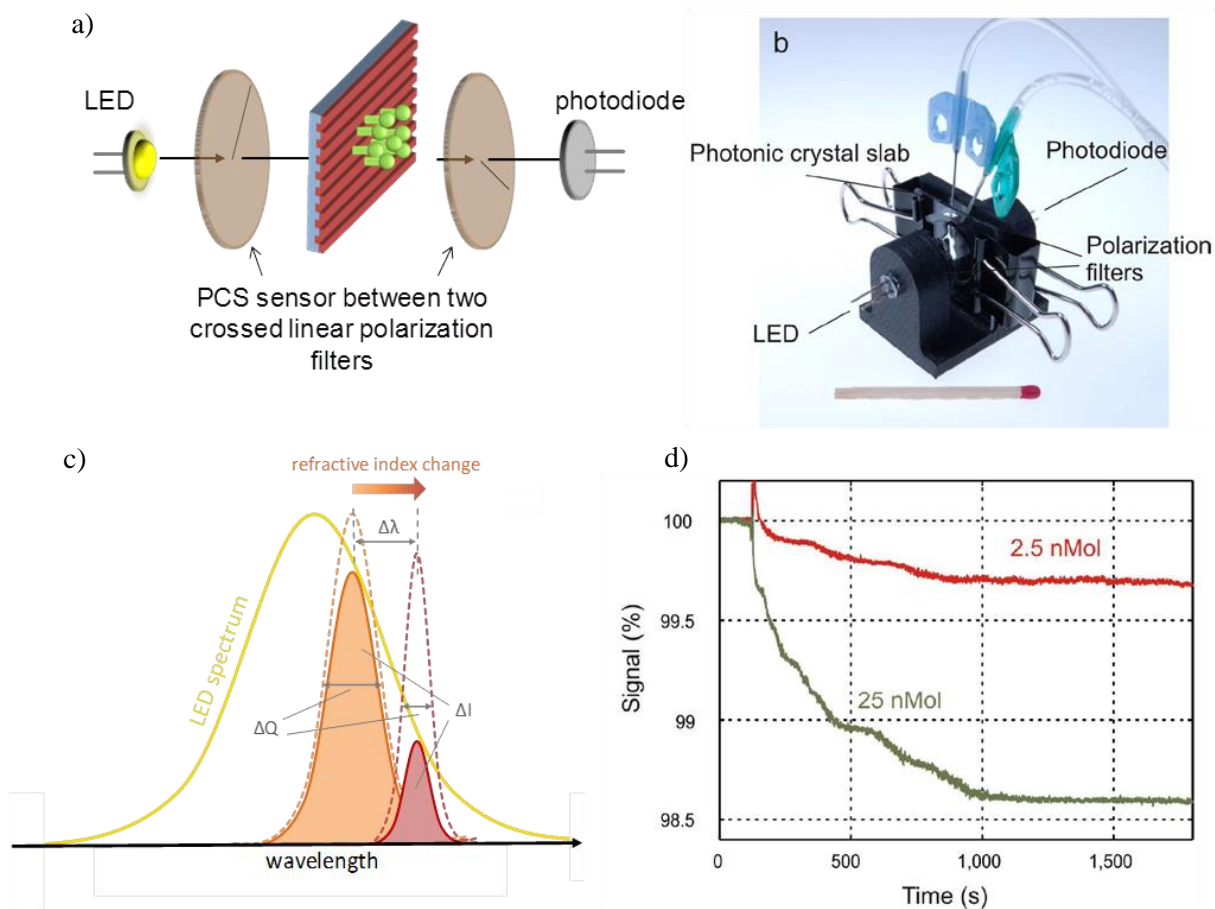
Figure 5: a) Single-channel intensity-based readout systems. An LED is used as light source and a photodiode as detector. The PCS is placed between two crossed linear polarizing filters. (b) Photograph of first prototype. Analyte is injected via the butterfly cannulas [reproduced from [27] with permission (will be obtained after acceptance of manuscript)]. (c) Working principle of intensity-based PCS readout. The resonance is placed on an edge of the LED spectrum. Thus, a change in resonance wavelength is converted to a change in the transmission (and reflection) intensity. d) Demonstration of detection of 2.5 nMol streptavidin with the match-size readout system shown in b) [reproduced from [27] with permission (will be obtained after acceptance of manuscript)].

3.2. 96-channel intensity-based PCS system

Based on the single-channel technology discussed in section 3.1, Nazirizadeh et al. demonstrated 2016 a 96-channel intensity-based reader for microtiter plates that has the same footprint as the microtiter plate [28]. The microtiter plates have a nanostructured bottom such as the one shown in figure 1c. The readout is performed using 96 optical channels consisting of an LED, a circular polarizing filter, and a photodiode as depicted in figure 6. This intensity-based system allows for both biochemical interaction analyses as well as cellular assays. The system does not use a spectrometer or moving mechanical parts allowing for the compact footprint.
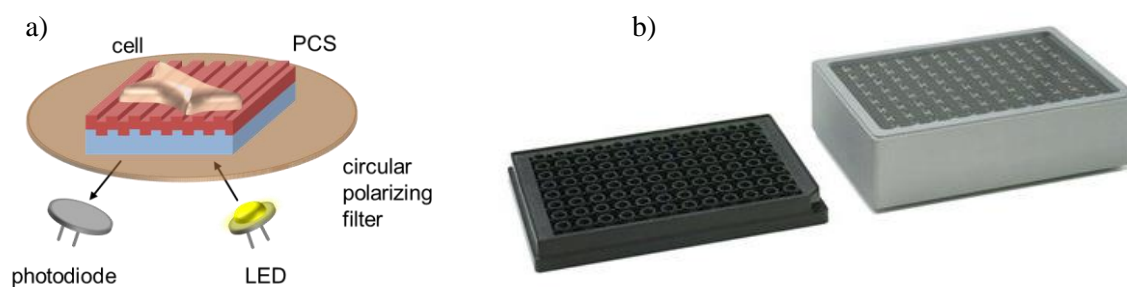

Figure 6: (a) Schematic of intensity-based cell assay. (b) Photograph of 96-channel intensity-based readout system with the same footprint as a microtiter plate [reproduced from [28] with permission (will be obtained after acceptance of manuscript)].

An important issue regarding intensity-based measurements of cellular assays is the changing cell scattering [28, 29]. In a cell adhesion and spreading experiment, first the scattering increases as the number of cells on the surface increases. As a continuous layer of cells is formed, the scattering decreases again. Mass redistribution in cells may as well change the scattering properties for the quasi-guided mode in the PCS. While the wavelength response is not influenced by scattering, the changed scattering causes a changed resonance peak width as well as a changed intensity signal. Therefore, the intensity signal in general is ambiguous in cell experiments. Nazirizadeh et al. demonstrate that choosing a guided-mode resonance near cutoff allows for an unambiguous response [28].

3.3. Portable, intensity-based imaging readout system

Towards an even more compact system with a high channel number, Jahns et al. realized an imaging camera-based reader system [30]. This imaging system is able to validate multiple and specific proteins for non-ambiguous diagnostics with single shot measurements. The system has an overall size of 13 cm x 4.9 cm x 3.5 cm (figure 7b). The PCS is locally functionalized by spotting of the receptor molecules. The sensor chip is placed between two crossed linear polarizers, a focusing, and a parallelizing lens (figure 7a). In this setup an LED with a bandwidth of 40 nm is used as excitation source. The TM resonance of the PCS is aligned to the falling edge of the LED spectrum as well as to the falling edge of the camera sensitivity in the green color channel, as depicted in figure 7c. Because of this imaging approach the whole PCS sensor surface with a diameter of 2 cm can be read out at the same time. By functionalizing the sensor surface locally, the specific and label-free detection of three different proteins at six receptor positions was demonstrated [30].
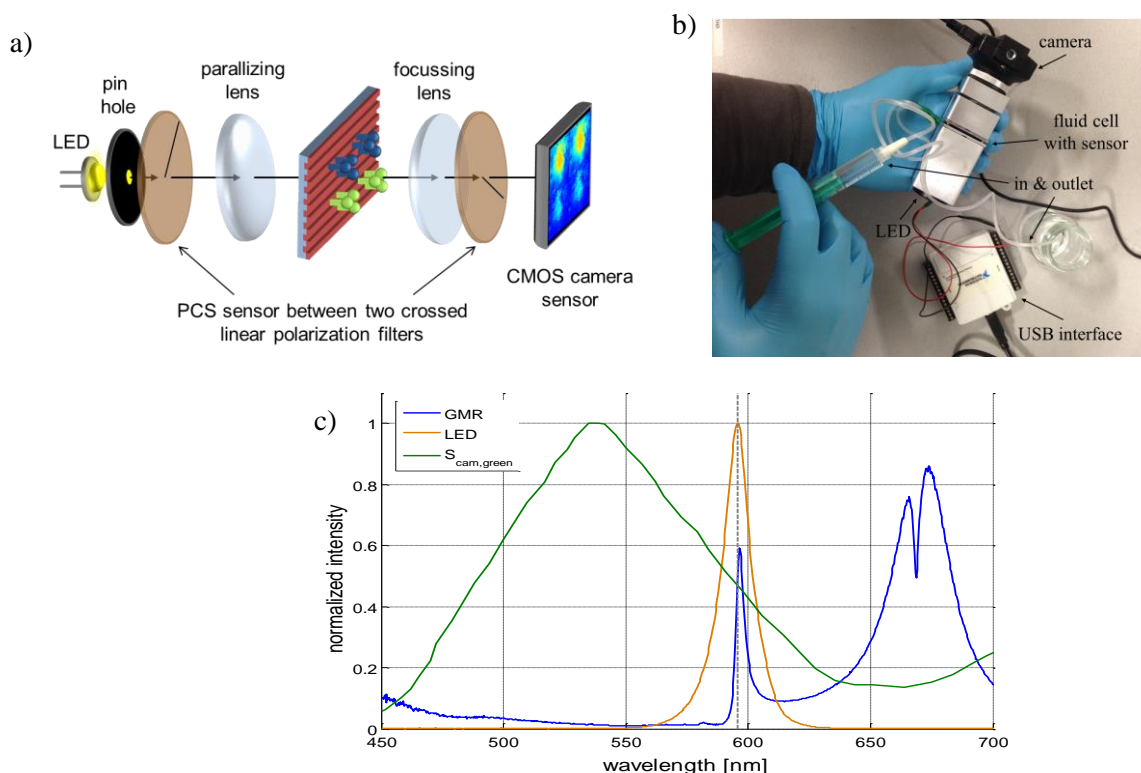

Figure 7: (a) Schematic of imaging readout system. (b) Photograph of photometric readout system with camera, LED, and optics within the metallic torso, the fluid cell with the biosensor, the butterfly cannulas for inlet and outlet and the USB-interface. (c) LED spectrum, camera sensitivity ($S_{cam,green}$), and PCS spectrum (GMR) with crossed polarization filters.

Figure 8 shows as an example a surface locally functionalized for detection of the CD40 ligand antibody (150 kDa). Six drops of the protein CD40 ligand dissolved in buffer were functionalized with a concentration of 1 μM as receptors on the PCS surface. During the protein detection experiment, first, pure buffer is placed inside a fluid cell to generate a baseline signal. After ten minutes, 90 nM of the protein CD40 ligand antibody dissolved in puffer is filled into the fluid cell. The camera continuously takes pictures of the PCS sensor surface. In figure 8a the last picture taken after protein association is subtracted from the first picture. The six binding positions are clearly visible as local intensity changes.

The intensity values within the binding positions M1-M6 are then background corrected with an in-house developed algorithm and plotted against time (Figure 8b) [30]. The association of the protein causes a corresponding intensity reduction showing typical binding kinetics. The nominally identical detection sites exhibit a different intensity response. We attribute this behavior to the experimental variation in the functionalization process. An automatic spotter should be used to guarantee identical spot sizes and receptor densities for the different sites.
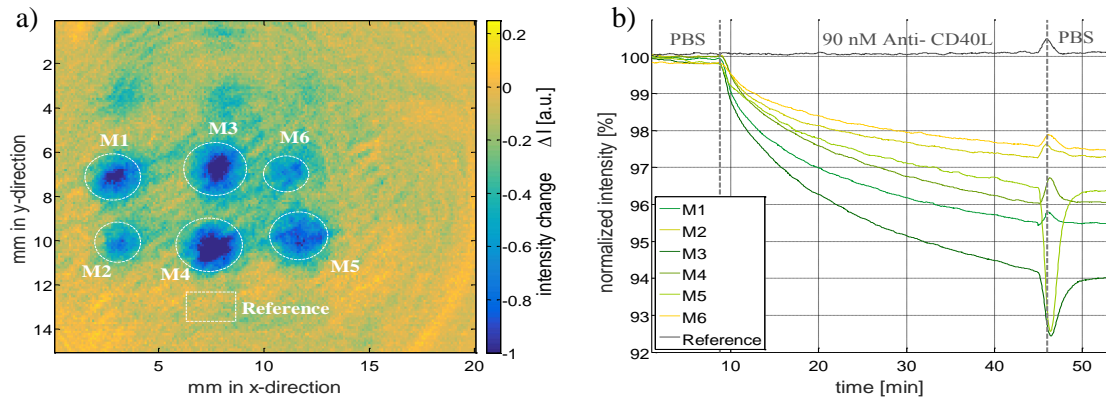

Figure 8: a) Difference intensity image with the reference and measurement fields marked with dashed white lines. b) Background-corrected intensity values plotted against time.

Regarding the resolution, it is feasible to place 20 x 20 = 400 receptor positions with 12 nl drops, an approximate spot diameter of 300 μm, and a pitch of 500 μm on a 1 cm² large sensor surface. For further miniaturization and high-Q samples the mode propagation in the waveguide needs to be considered [31, 32]. The imaging approach does not require scanning and thus allows reliable and fast, time-resolved measurement results. The demonstrated system limit of detection of 168 pM (24 ng/ml) is already suitable to identify several relevant biomarker concentrations [30]. For a broader application range, the signal-to-noise ratio needs to be further enhanced to be able to detect concentrations in the range of pg/ml.

4. Multiperiodic and Aperiodic Nanostructures

This section reviews advanced nanostructures for resonant-waveguide-grating biosensors beyond simple monoperiodic gratings. We present two different concepts of nanostructure designs: compound multiperiodic gratings and deterministic aperiodic nanostructures. Both recently have been suggested for refractive index biosensors [33-35].

Compound gratings are obtained by a superposition of multiple monoperiodic gratings, e.g., by performing a logical disjunction operation. Each period adds peaks to the spectrum. Thus, compound multiperiodic gratings allow the design of number and wavelengths of guided-mode resonances (GMRs) in the transmission and reflection spectrum. By tuning the duty cycle, the relative intensities of the resonance peaks may be tailored [36]. Figure 9 shows the measured transmission spectra of two different multiperiodic PCSs with transverse-electric excitation. The gratings consist of two and three grating periods (2-compound: 250 nm and 300 nm, 3-compound: 250 nm, 300 nm and 350 nm), each having a distinct resonance dip in the spectrum. The fabrication and experimental characterization are described in detail in [25, 30]. The additional peaks in the spectrum are promising for multi-LED intensity-based readout systems allowing for further improvements in the signal-to-noise ratio.
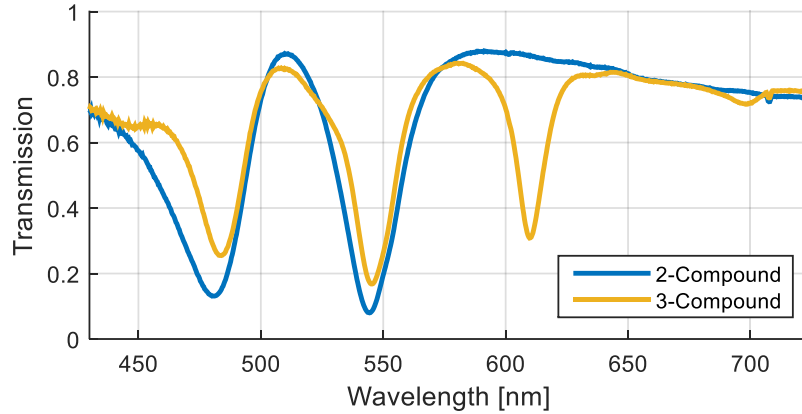
Figure 9: Experimental TE transmission spetra of two multiperiodic resonant waveguide gratings. The 2-compound grating has periods of 250 nm and 300 nm superimposed, the 3-compound grating has periods of 250 nm, 300 nm, and 350 nm.

The second design concept of deterministic aperiodic nanostructures (DANS) employs the idea to introduce disorder to the grating layer. Disordered, dielectric media have been shown to feature high field concentrations due to localization effects [37] and high quality resonances have been reported. Deterministic aperiodic sequences are generated by mathematical substitution rules. While being non-periodic, they feature self-similarity at different orders and thus allow for guided mode resonances when employed as a diffraction layer within the waveguide. We investigated three different aperiodic nanostructures based on the Rudin-Shapiro, the Thue-Morse, and the Fibonacci sequence. These three examples are chosen for their different degrees in disorder. The Rudin-Shapiro nanostructure, having a continuous spatial Fourier spectrum, has the highest disorder, while Thue-Morse and Fibonacci nanostructures have less disorder, featuring singular-continuous and pure-point, Bragg-like spatial Fourier spectra [38, 39]. The three different aperiodic sequence substitution rules are given in table 1. To create a nanostructured grating from the binary sequences, the letters of the calculated sequences are translated into 50-nm wide ridges for an A and 50-nm wide grooves for a B as depicted in figure 10 [35]. Figure 11 shows images of the three different grating structures taken by a scanning electron microscope (SEM).

Table 1
Overview of discussed nanostructures

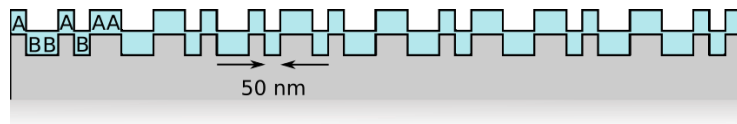| Name	Type	Substitution rules
Rudin-Shapiro	High disorder, continuous spectrum	AA → AAAB, AB → AABA, BA → BBAB, BB → ABBA
Thue-Morse	Medium disorder, singular continuous spectrum	A →AB, B → BA
Fibonacci	High order, pure-point spectrum	A → AB, B → A

Figure 10: Principle of deterministic aperiodic nanostructured waveguide. The binary symbols of the aperiodic sequence are translated into ridges (A) and grooves (B) with 50 nm lateral width.
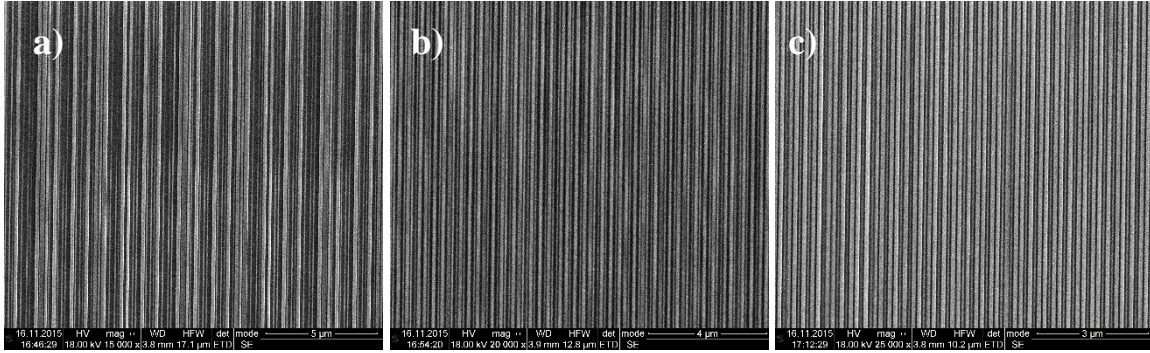
Figure 11: Scanning electron microscope images of the Rudin-Shapiro (a), Thue-Morse (b), and Fibonacci (c) nanostructures on the nickel shim master.

Measured TE transmission spectra for three samples based on the above mentioned sequences are shown in figure 12. The spectrum of the sample based on the Rudin-Shapiro sequence shows many ripples over the visible spectrum that may be contributed to the continuous Fourier spectrum. Resonances are not clearly distinguishable and also the intensities are low. The resonances of the Thue-Morse sample show a higher reflectivity, but again the resonances are not as distinct as the resonances of Bragg gratings. Here the Fibonacci sample shows the most distinct resonances corresponding to two peaks in the spatial Fourier spectrum.
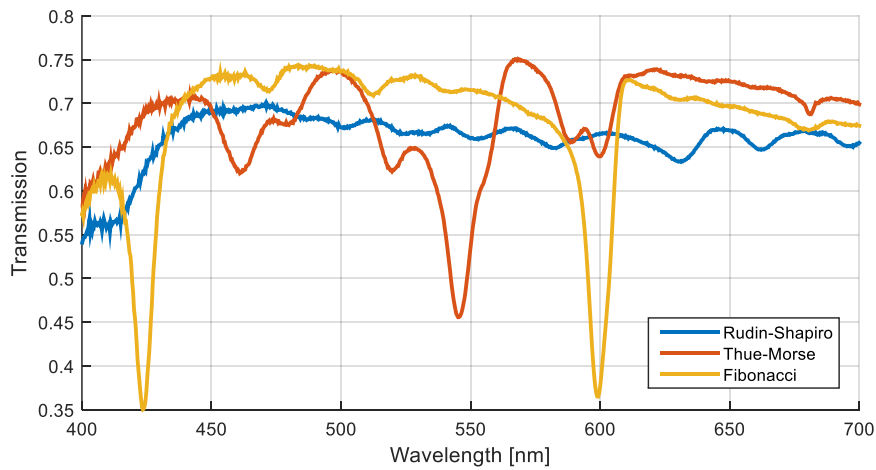

Figure 12: Experimental TE resonance spectra of three nanostructured dielectric waveguides with different deterministic aperiodic nanostructures based on Rudin-Shapiro, Thue-Morse, and Fibonacci binary sequences in water (1.33).

For analyzing the sensitivity of aperiodic nanostructured waveguides we consider experimental results for step-wise changes of the analyte refractive index. The nanostructured waveguides are placed into a fluid cell and water-glycerol mixtures with changing composition are injected into the fluid cell. The refractive index is varied from 1.33 (water) to 1.389 by mixing water with glycerol in 5% steps. For each refractive index step and each nanostructure under investigation 100 spectra are recorded within 50 s. After each step the fluid cell is flushed with distilled water and another 100 reference spectra are recorded. The recorded spectra are normalized to the excitation spectrum of the setup and dip positions in the spectrum are obtained by a parabolic fit. The mean resonance position of the 100 recorded spectra is calculated. Figure 13 shows the time sequences of the resonance positions during the experiments. Particularly interesting is the different noise behavior of the different resonances. The noise is a combined effect of the signal-to-noise ratio of the hardware and the performance of the resonance tracking algorithm.
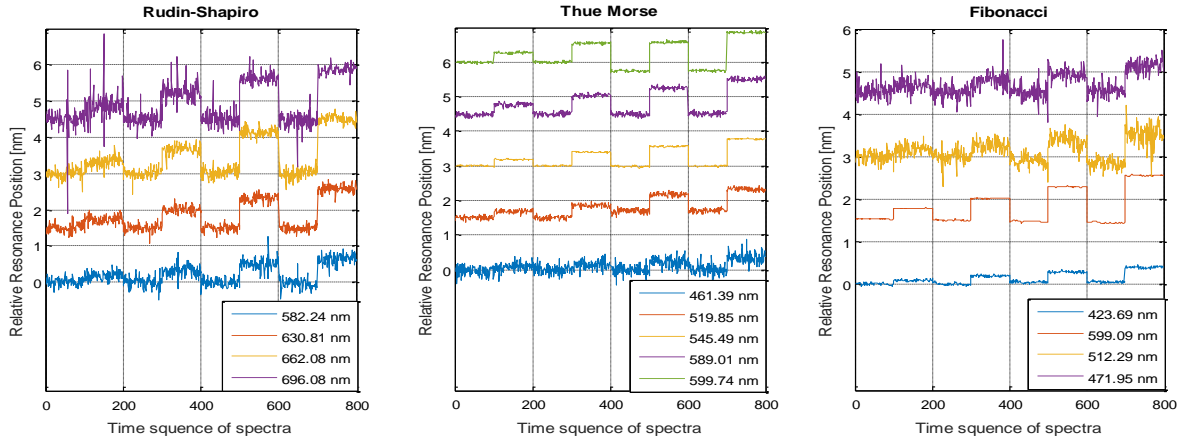
Figure 13: Measured relative resonance positions for different resonances of three deterministic aperiodic nanostructured waveguides. The time sequence of measured spectra is plotted (100 per refractive index step). The average resonance wavelength of the first 100 spectra is subtracted for each dip and the curves are offset by 1.5 nm for better visibility. The bulk refractive index in the analyte region is changed in the following steps water – water/5% glycerol – water - water/10% glycerol – water – water/15% glycerol – water - water/20% glycerol.

The change in resonance position with refractive index change is plotted in figure 14. It is observed that different resonances show different sensitivities. Table 2 summarizes the calculated sensitivity, the standard deviation, and the limit of detection for each resonance under investigation. The limit of detection is calculated as the quotient of the standard deviation σ and the sensitivity S:

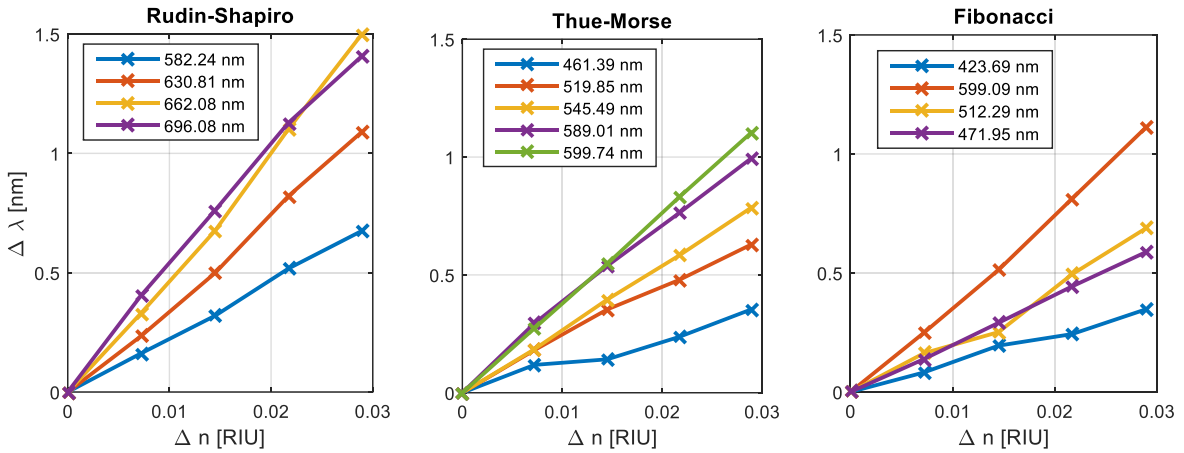$$LOD = \frac{3 \cdot \sigma}{S} \qquad (5)$$

Figure 14: Measured resonance shifts for multiple resonances in the spectrum of three different aperiodic nanostructured waveguides. The bulk refractive index in the analyte region is changed from water (1.33) to 20% glycerol concentration (1.359).

The resonances of the Rudin-Shapiro sample offer the highest resonance shifts, up to 1.5 nm for a change of 0.029 RIU. Its sensitivities range from 23 to 51 nm/RIU. Because the resonance peaks are weak, there is a higher noise in the resonance positions leading to worse limits of detection compared to the Thue-Morse sample. The resonance shifts of the Thue-Morse and Fibonacci sample are in the range 0.3 nm to 1.2 nm for the chosen change in refractive index.

Table 2:
Measured sensitivities and limits of detection for different resonances of three aperiodic nanostructured waveguides

Name	Resonance position [nm]	Sensitivity [nm/RIU]	Standard deviation [nm]	Limit of Detection [RIU]
Rudin-Shapiro	582.2	23.35	0.1347	$17.3 \cdot 10^{-3}$
	630.8	37.68	0.1036	$8.2 \cdot 10^{-3}$
	662.0	48.69	0.1012	$6.2 \cdot 10^{-3}$
	696.0	51.83	0.1080	$6.3 \cdot 10^{-3}$
Thue-Morse	461.3	12.23	0.1487	$36.65 \cdot 10^{-3}$
	519.8	21.76	0.0460	$6.3 \cdot 10^{-3}$
	545.4	27.17	0.0106	$1.1 \cdot 10^{-3}$
	589.0	34.41	0.0454	$4.0 \cdot 10^{-3}$
	599.7	38.17	0.0217	$1.7 \cdot 10^{-3}$
Fibonacci	423.6	12.00	0.0206	$5.2 \cdot 10^{-3}$
	471.9	20.31	0.1365	$20.2 \cdot 10^{-3}$
	512.2	23.77	0.2319	$29.3 \cdot 10^{-3}$
	599.2	38.40	0.0110	$1.6 \cdot 10^{-3}$

In general, the resonances at higher wavelengths show higher sensitivities, which can be attributed to the more extended evanescent field (fig. 4 (a)). This effect also explains the highest sensitivities of the Rudin-Shapiro sequence. Figure 15 plots the measured sensitivities over the absolute resonance position. A linear correlation is obtained from the measured data.
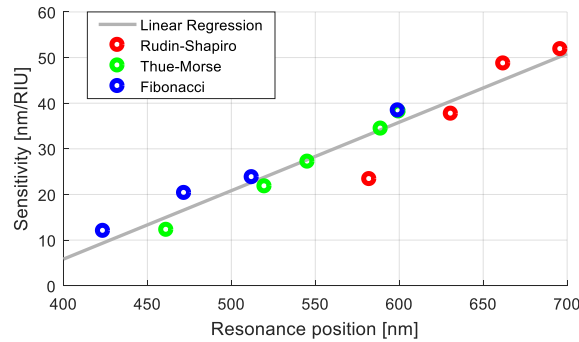

Figure 15: Bulk sensitivities of different guided-mode resonances of deterministic aperiodic nanostructured waveguide gratings. Grey line is a linear fit to the data points.

Both with the compound-grating nanostructures and the deterministic aperiodic nanostructures new opportunities are obtained for designing the spectral characteristics. This allows for new multi-LED intensity-based detection systems. The observed bulk sensitivity is similar to the one observed in monoperiodic gratings [35]. On the other hand, exciting new opportunities open with highly localized fields with high field intensities [37]. To take advantage of these localized modes for highly sensitive biosensors, schemes for localized functionalization need to be implemented, i.e., receptor sites for target molecules should only be placed in high-field areas. This localized functionalization will improve both the performance of traditional spectrometer-based readout systems as well as of intensity-based readout systems.

5. Summary and Outlook

We reviewed progress in intensity-based reader systems for resonant waveguide grating (RWG) biosensors. The transmission and reflection spectrum of an RWG are linked to the refractive index distribution in the analyte region above the RWG. Changes of the refractive index caused by biomolecular binding or by a change of the cell number or cellular mass distribution in a cellular assay cause a shift of the guided-mode resonance (GMR) in the spectrum. Here, the biosensor is only sensitive to changes of refractive index within the penetration depth of quasi-guided modes.

In an intensity-based reader, the spectral change is converted to a change in transmitted or reflected intensity by positioning the GMR on an intensity edge of the spectral response. This measurement

principle requires no mechanical scanning and no spectrometer. Single-channel readers, 96-well microtiter plate readers, as well as an imaging camera-based reader have been discussed. The readout system has a size of 13 cm x 4.9 cm x 3.5 cm. The system has a signal-to-noise ratio corresponding to a limit of detection of 168 pM (24 ng/ml). These results show the potential of intensity-based reader systems for point-of-care applications.

Future development towards a high channel count test chip with imaging readout needs to address two aspects in particular: further improvement in signal-to-noise ratio as well as the practical realization of the disposable test chip. For improving the signal-to-noise ratio an in-depth analysis of the noise sources should be carried out. Here, results obtained for microresonator-based sensors form a basis for the investigation [40, 41]. The noise sources in RWG biosensors should be compared to these results and intrinsic noise sources need to be identified to determine the intrinsic noise floor. We reviewed recent research on advanced nanostructure designs for improved signal detection. It was shown that compound grating nanostructures and deterministic aperiodic nanostructures allow for the design of the spectral features. These investigations show that, for example, a three-LED intensity-based reader could be designed. Here, the LEDs should have non-overlapping spectra and one resonance should be at either the rising or the falling edge of each LED. With this concept, new opportunities for self-calibration arise. The local functionalization with receptor sites corresponding to the locally-enhanced electric field in deterministic aperiodic nanostructures is another promising route toward systems with higher sensitivity.

For the disposable test chip the separate design and combination of a microfluidic chip with a nanostructured and biofunctionalized functional chip appears most promising. Here, the microfluidic chip needs to be designed for sample introduction and filtering as well as for fluid delivery to the functional chip. This microfluidic chip may be fabricated cost effectively by injection molding. The nanostructuring of the functional chip is feasible by nanoimprint lithography. The subsequent biofunctionalization needs to be performed under well-controlled conditions to prevent degradation. The microfluidic chip and the functional chip may be combined by adhesives with tightness still being an unresolved issue. For a 1 cm² large sensor surface of the functional chip 400 separate receptor positions are feasible.

The second large application area opening up for intensity-based readout of RWG biosensors is compact reader systems for cellular assays. Intensity-based readout of cellular assays in a nanostructured microtiter plate has been demonstrated successfully. Due to the small system size, potentially many each microtiter plate may be monitored with its own intensity-based reader underneath. Furthermore, intensity-based systems are small enough to be integrated into incubators. Thus, the systems have the potential for continuous monitoring of cellular assays and high-throughput analysis.

Acknowledgements

References
[1] J. McCord, R. M. Nowak, P. A. McCullough, C. Foreback, S. Borzak, G. Tokarski, M. C. Tomlanovich, G. Jacobsen, W. D. Weaver, Ninety-Minute Exclusion of Acute Myocardial Infarction By Use of Quantitative Point-of-Care Testing of Myoglobin and Troponin I, Circulation 104(13) (2001) 1483–1488.

[2] M. B. Schulze, K. Hoffmann, H. Boeing, J. Linseisen, S. Rohrmann, M. Möhlig, A. F. H. Pfeiffer, J. Spranger, C. Thamer, H.-U. Häring, A. Fritsche, H.-G. Joost, An Accurate Risk Score based on Anthropometric, Dietary, and Lifestyle Factors to Predict the Development of Type 2 Diabetes, Diabetes Care 30(3) (2007) 510–515.

[3] J. Fritz, Cantilever biosensors, Analyst 133 (2008) 855–863.

[4] J. A. Lee, S. Hwang, J. Kwak, S. Il Park, S. S. Lee, K. C. Lee, An electrochemical impedance biosensor with aptamer-modified pyrolyzed carbon electrode for label-free protein detection, Sensors Actuators B 129(1) (2008) 372–379.

[5] M. A. Cooper, Optical biosensors in drug discovery, Nat. Rev. Drug Discov. 1(7) (2002) 515–528.

[6] K. Länge, B. E. Rapp, M. Rapp, Surface acoustic wave biosensor: a review, Anal. Bioanal. Chem 391 (2008) 1509-1519.

[7] A. Waggoner, Fluorescent labels for proteomics and genomics, Curr. Opin. Chem. Biol. 10(1) (2006) 62–66.

[8] X. Fan, I. M. White, S. I. Shopova, H. Zhu, J. D. Suter, Y. Sun, Sensitive optical biosensors for unlabeled targets: A review, Anal. Chim. Acta 620(1-2) (2008) 8–26.

[9] R. Bruck, E. Melnik, P. Muellner, R. Hainberger, M. Lämmerhofer, Integrated polymer-based Mach-Zehnder interferometer label-free streptavidin biosensor compatible with injection molding, Biosens. Bioelectron. 26(9) (2011) 3832–3837.

[10] C. L. Wong, M. Olivo, Surface Plasmon Resonance Imaging Sensors: A Review, Plasmonics 9 (20154) 809–824.

[11] H. K. Hunt, A. M. Armani, S. Member, Bioconjugation Strategies for Label-Free Optical Microcavity Sensors, IEEE J. Sel. Top. Quantum Electron. 20(2) (2014) 121-133.

[12] D. Threm, Y. Nazirizadeh, M. Gerken, Photonic Crystal Biosensors towards On-Chip Integration, J. Biophotonics 5(8 – 9) (2012) 601 - 616.

[13] Y. Fang, Label-free cell-based assays with optical biosensors in drug discovery, Assay Drug Dev. Technol. 4(5) (2006) 583–595.

[14] I. D. Block, P. C. Mathias, S. I. Jones, L. O. Vodkin, B. T. Cunningham, Optimizing the spatial resolution of photonic crystal label-free imaging, Appl. Opt. 48(34) (2009) 6567.

[15] H. Inan, M. Poyraz, F. Inci, M.A. Lifson, M. Baday, B.T. Cunningham, and U. Demirci, Photonic Crystals: Emerging biosensors for point-of-care applications, Chem. Soc. Rev. 46 (2017) 366-388.

[16] B. T. Cunningham, M. Zhang, Y. Zhuo, L. Kwon and C. Race, Recent Advances in Biosensing With Photonic Crystal Surfaces: A Review, IEEE Sens. J. 16(10) (2016) 3349-3366.

[17] S. Fan, J. Joannopoulos, Analysis of guided resonances in photonic crystal slabs, Phys. Rev. B 65(23) (2002) 1–8.

[18] D. Rosenblatt, A. Sharon, A. A. Friesem, Resonant grating waveguide structures, IEEE J. Quant. Electron. 33(11) (1997) 2038-2059.

[19] G. A. Turnbull, P. Andrew, M. J. Jory, W. L. Barnes, and I. D. W. Samuel, Relationship between photonic band structure and emission characteristics of a polymer distributed feedback laser, Phys. Rev. B 64 (2001) 125122.

[20] J. Yang, H. Giessen, P. Lalanne, Simple analytical expression for the peak-frequency shifts of plasmonic resonances for sensing, Nano Lett. 15(5) (2015) 3439-3444.

[21] Y. Nazirizadeh, U. Lemmer, M. Gerken, Experimental quality factor determination of guided-mode resonances in photonic crystal slabs, Appl. Phys. Lett. 93 (2008) 261110-261112.

[22] R. Horvath, L. R. Lindvold, N. B. Larsen, Reverse-symmetry waveguides: theory and fabrication, Appl. Phys. B 74(4) (2002) 383-393.

[23] I. D. Block, N. Ganesh, M. Lu, B. T. Cunningham, A Sensitivity Model for Predicting Photonic Crystal Biosensor Performance, IEEE Sens. J. 8(3) (2008) 274–280.

[24] Y. Nazirizadeh, F. von Oertzen, K. Plewa, N. Barié, P-J. Jakobs, M. Guttmann, H. Leiste, M. Gerken, Sensitivity optimization of injection-molded photonic crystal slabs for biosensing applications, Opt. Mat. Express 3(5) (2013) 556-565.

[25] M. Paulsen, L. T. Neustock, S. Jahns, J. Adam, M. Gerken, Simulation methods for multiperiodic and aperiodic nanostructured dielectric waveguides, Opt. Quant. Electron. 49 (2017) 107.

[26] H.-Y. Wu, W. Zhang, P. Mathias, B. Cunningham, Magnification of photonic crystal fluorescence enhancement via TM resonance excitation and TE resonance extraction on a dielectric nanorod surface, Nanotechnology 21 (2010) 125203-125209.

[27] Y. Nazirizadeh, U. Bog, S. Sekula, T. Mappes, U. Lemmer, M. Gerken, Low-cost label-free biosensors using photonic crystals embedded between crossed polarizers, Opt. Express 18(18) (2010) 19120-19128.

[28] Y. Nazirizadeh, V. Behrends, A. Prósz, N. Orgovan, R. Horvath, A. M. Ferrie, Y. Fang, C. Selhuber-Unkel, M. Gerken, Intensity interrogation near cutoff resonance for label-free cellular profiling, Sci. Rep. 6 (2016) 24685.

[29] Y. Fang, A. M. Ferrie, N. H. Fontaine, J. Mauro, J. Balakrishnan, Resonant waveguide grating biosensor for living cell sensing, Biophys. J. 91 (2006) 1925–1940.

[30] S. Jahns, M. Bräu, B. O. Meyer, T. Karrock, S. B. Gutekunst, L. Blohm, C. Selhuber-Unkel, R. Buhmann, Y. Nazirizadeh, M. Gerken, Handheld Imaging Photonic Crystal Biosensor for Multiplexed, Label-Free Protein Detection, Biomed. Opt. Express 6(10) (2015) 3724-3736.

[31] I. D. Block, P. C. Mathias, S. I. Jones, L. O. Vodkin, and B. T. Cunningham, Optimizing the spatial resolution of photonic crystal label-free imaging, Appl. Opt. 48(34) (2009) 6567–6574.

[32] G. J. Triggs, M. Fischer, D. Stellinga, M. G. Scullion, G. J. O. Evans, and T. F. Krauss, Spatial Resolution and Refractive Index Contrast of Resonant Photonic Crystal Surfaces for Biosensing, in IEEE Photo. J. 7(3) (2015) 1-10.

[33] S. V. Boriskina, L. Dal Negro, Sensitive label-free biosensing using critical modes in aperiodic photonic structures, Opt. Express 16 (2008) 12511-12522.

[34] L. Dal Negro, Enhancing optical biosensing with aperiodicity, SPIE Newsroom (2012).

[35] L. T. Neustock, S. Jahns, J. Adam, M. Gerken, Optical waveguides with compound multiperiodic grating nanostructures for refractive index sensing, J. of Sens. 501 (2015) 6174527.

[36] C. Kluge, J. Adam, N. Barié, P. J. Jakobs, M. Guttmann, M. Gerken, Multiperiodic nanostructures for photon control, Opt. Express 22 (2014) A1363-A1371.

[37] S. V. Boriskina, A. Gopinath, L. Dal Negro, Optical gap formation and localization properties of optical modes in deterministic aperiodic photonic structures, Opt. Exp. 16 (2008) 18813.

[38] L. Dal Negro, S.V. Boriskina, Deterministic aperiodic nanostructures for photonics and plasmonics applications, Laser Photon. Rev. 6(2) (2012) 178-218.

[39] E. Maciá, Exploiting aperiodic designs in nanophotonic devices, Rep. Prog. Phys. 75 (2012) 036502.

[40] J. Knittel, J. D. Swaim, D. L. McAuslan, G. A. Brawley, and W. P. Bowen, Back-scatter based whispering gallery mode sensing, Sci. Rep. 3 (2013) 2974.

[41] X. Zhou, L. Zhang, and W. Pang, Performance and noise analysis of optical microresonator-based biochemical sensors using intensity detection. Opt. Exp. 24(16), (2016) 18197-18208.